Grain Boundary Solute Drag Model in Regular Solution Alloys

Malek Alkayyali[1] and Fadi Abdeljawad[1,2,*]
[1]Department of Mechanical Engineering, Clemson University, Clemson, South Carolina 29634, USA
[2]Department of Materials Science and Engineering, Clemson University, Clemson, South Carolina 29634, USA

(Received 23 August 2021; revised 16 September 2021; accepted 27 September 2021; published 22 October 2021)

We present a grain boundary (GB) solute drag model in regular solution alloys. The model accounts for solute-solute interactions in both the bulk and GBs and captures effects such as monolayer, multilayer, and asymmetrical segregation. Our analysis shows that deviations from ideal solution thermodynamics play a paramount role, in which solute drag is shown to scale with solute-solute interaction parameters. Further, it is found that the asymmetry in GB segregation introduces an additional component to solute drag. A universal solute drag-GB velocity relation is proposed and used to explain recent experimental observations of sluggish grain growth in a wide range of engineering alloys.

DOI: 10.1103/PhysRevLett.127.175503

Motivation.—Nearly all structural and functional materials are polycrystalline aggregates. They are composed of crystalline grains that are joined at internal interfaces, termed grain boundaries (GBs) [1]. It is well accepted that GB dynamical processes play a pivotal role in controlling the formation and evolution of microstructure and, as a result, many crystal-size dependent materials properties, such as mechanical strength [2,3] and transport [4,5]. Even minute amounts of intended or unintended impurities at GBs result in profound changes to GB dynamics. The preferential segregation of elemental species to GBs has been found to influence materials phenomena, including diffusion [6], GB cohesion and embrittlement [7], and activated sintering [8,9]. Of particular interest is the role that GB solute segregation plays in grain growth, in which curvature-driven GB migration is expressed using the following for the normal velocity $\mathcal{V}$ of the GB [10]

$$\mathcal{V} = M_{\mathrm{GB}} \Delta P = M_{\mathrm{GB}} \gamma_{\mathrm{GB}} \mathcal{K}. \tag{1}$$

Here, M_{GB} is the GB mobility and $\Delta P = \gamma_{\mathrm{GB}} \mathcal{K}$ is the driving force for GB migration, where γ_{GB} is the GB energy and $\mathcal{K}$ is the local interface mean curvature. Two primary mechanisms contribute to the migration of doped GBs. The first is thermodynamic, described using the Gibbs adsorption equation [11,12]. The segregation of an alloying element to a GB at a given temperature and pressure leads to the reduction of GB energy and, thus, the driving force for GB migration. The second effect is kinetic, termed solute drag. Segregated solutes will attempt to remain within the GB and, as a result, the migrating GB has to drag solute atoms, creating a drag force [13,14]. Indeed, recent experimental studies have demonstrated GB solute segregation as a mechanism to mitigate grain coarsening in a wide range of nanocrystalline alloys [15–20]. However, much of our current understanding has been focused on the thermodynamic aspect of GB segregation, and the role of solute drag remains poorly understood. This, in part, is due to the fact that existing solute drag treatments employ several restrictive assumptions severely limiting their ability to quantitatively predict the impact of solute drag on GB migration. Existing solute drag treatments employ ideal and dilute alloy thermodynamics [13] or do not account for solute-solute interactions within GBs [21,22]. However, recent studies revealed heavily doped GBs with solute levels that are too high to be considered ideal [17,18,23–25]. Such studies highlight the need to account for GB solute-solute interactions, which can be attractive or repulsive, and are, in principle, different from those in the bulk grains. For example, atomistic simulations of the free energy of a $\Sigma 5(310)$ GB in a model Cu-Ag system revealed repulsive GB solute-solute interactions over some range of Ag concentrations [26]. Very recently, a discrete model of GB phase transformations and segregation has been proposed and used to demonstrate the impact of GB phases on boundary mobility [27]. In addition, the aforementioned solute drag treatments assume monolayer and symmetric segregation profiles; an assumption that is only valid for a small subset of GBs. Multilayer segregation has been experimentally observed in a wide range of metallic alloys [28,29]. Xie *et al.* [30] revealed asymmetrical solute segregation to tilt GBs in a Mg-based alloy. The goal of this Letter, therefore, is to present a GB solute drag model in regular solution alloys that accounts for solute-solute interactions in both bulk and GBs and captures effects such as multilayer and asymmetrical segregation.

Model.—In this Letter, we consider a one-dimensional bicrystal system with semi-infinite grains, where the first grain extends in the region $x \in (-\infty, -\delta)$, and the second one is defined over $x \in (+\delta, +\infty)$, resulting in a GB width of 2δ. The starting point of our treatment is the introduction of a spatially varying indicator function $\Upsilon(x)$ used to locate

the GB region and define solute-GB interactions. $\Upsilon = 0$ in the bulk grains and peaks to a value of one within the GB region. Two canonical functional forms for Υ are explored in this Letter, representing a wide range of possible GB segregation profiles. The first is a smoothed boxcar function, which results in a GB with multilayer segregation, and the second is a skew-normal (sn) function used to account for asymmetrical GB segregation. The functional forms for $\Upsilon(x)$ are given by

$$\Upsilon = \begin{cases} \frac{1}{2}\left[\tanh\left(\frac{x+\epsilon}{\rho}\right) - \tanh\left(\frac{x-\epsilon}{\rho}\right)\right], & \text{boxcar} \\ \frac{2\beta}{\omega}\phi\left(\frac{x-\xi}{\omega}\right)\Phi\left(\alpha\left(\frac{x-\xi}{\omega}\right)\right), & \text{skew normal,} \end{cases} \tag{2}$$

where $(\epsilon, \rho) = (0.8\delta, 0.1\delta)$ are the boxcar function parameters used to define Υ over the GB width 2δ. For the skew-normal function, $\phi(x) = \exp[-x^2/2]/\sqrt{2\pi}$, $\Phi(x) = [1 + \mathrm{erf}(x/\sqrt{2})]/2$, and ξ, ω, and α are parameters controlling its mean, variance, and skewness γ_{sn} [31]. Here, we note that $\alpha = 0$ reduces to the standard Gaussian. Letting $\eta = (\sqrt{2/\pi})\alpha/\sqrt{1+\alpha^2}$, $\gamma_{\mathrm{sn}} = (4-\pi)\eta^3/[2(1-\eta^2)^{3/2}]$ [31], and we set $\beta = (\omega/2)/\max(\phi\Phi)$, so Υ peaks at one within the GB region. In this study, we explore three cases for the skew-normal Υ function: a symmetric Gaussian with $(\xi, \omega, \alpha) = (0, \delta/\sqrt{8}, 0)$ and left- and right-skewed functions with $(\xi, \omega, \alpha) = (\pm 0.81\delta, 0.58\delta, \mp 10)$. Figure 1 shows a schematic representation of the four Υ functions used in this work. The Gaussian and boxcar functions represent symmetric monolayer and multilayer segregation, respectively, whereas the left-skewed (right-skewed) function accounts for strong segregation on the leading (trailing) end of the migrating GB [traveling left to right according to Fig. 1]. Next, we use a solute concentration field $c(x,t)$ to describe bulk $f_b(c,T)$ and GB $f_{\mathrm{GB}}(c,T)$ free energies, where T is the absolute temperature. To account for solute-solute interactions within both the bulk and GB regions, we employ regular solution thermodynamics for the functional form of the free energy, which is given by [32]

$$f_i = G_i^B c + G_i^A(1-c) + k_B T[c\ln(c) + (1-c)\ln(1-c)] + \Omega_i c(1-c), \qquad i = \mathrm{GB}, b, \tag{3}$$

where $G^A(G^B)$ describes the free energy of pure solvent A (solute B) and k_B is Boltzmann constant. Ω_b and Ω_{GB} are the regular solution, or heat of mixing, model parameters for the bulk grains and GBs, respectively. The total free energy of the system is written as $f_{\mathrm{tot}} = \Upsilon f_{\mathrm{GB}} + (1-\Upsilon) f_b$, where Υ is used to interpolate the free energy between the bulk grains and GBs. The resultant chemical potential $\mu = \mu_B - \mu_A = \partial f_{\mathrm{tot}}/\partial c$ is then given by

$$\mu = G_b^B - G_b^A + k_B T \ln\left(\frac{c}{1-c}\right) + \Omega_b(1-2c) - (G_* + 2\Omega_* c)\Upsilon, \tag{4}$$

where $\Omega_* = \Omega_{\mathrm{GB}} - \Omega_b$ and $G_* = \Delta G^A - \Delta G^B - \Omega_*$. $\Delta G^A = G_{\mathrm{GB}}^A - G_b^A \propto \gamma_{\mathrm{GB}}^A A_{\mathrm{GB}}$ and $\Delta G^B = G_{\mathrm{GB}}^B - G_b^B \propto \gamma_{\mathrm{GB}}^B A_{\mathrm{GB}}$, where $\gamma_{\mathrm{GB}}^A(\gamma_{\mathrm{GB}}^B)$ is the GB energy of pure $A(B)$ and A_{GB} is the GB area. Ω_* describes the deviation of the GB heat of mixing parameter from the bulk one, where $\Omega_* < 0$ corresponds to immiscible alloys (i.e., $\Omega_b > 0$) and/or ones with GBs that act as preferential sites for A-B mixing (i.e., $\Omega_{\mathrm{GB}} < 0$). A close examination of Eq. (4) reveals that the coupling between the migrating GB and concentration field is described by a concentration-dependent interaction energy $E = -[G_* + 2\Omega_* c(x)]\Upsilon(x)$, in contrast to existing solute drag treatments, which assume a concentration-independent interaction energy [13,21]. Next, gradients in the chemical potential result in a mass flux given by $j = -[Dc(1-c)/k_BT]\partial\mu/\partial x$, where $c(1-c)/k_BT$ arises from the thermodynamic factor [33]. D is the solute diffusion in the direction of the migrating GB and is expressed as $D(x) = D_o\Upsilon(x)$, where D_o is a reference GB diffusivity. The steady state solute transport equation expressed in a frame moving with the GB at a constant velocity $\mathcal{V}$ is given by

$$\frac{\partial}{\partial x}\left[\frac{D_o \Upsilon c(1-c)}{k_B T}\frac{\partial \mu}{\partial x}\right] + \mathcal{V}\frac{\partial c}{\partial x} = 0. \tag{5}$$

Using the GB half-width δ and thermal energy of the system k_BT as reference length and energy scales, respectively, the above transport equation can be made nondimensional by letting $\bar{x} = x/\delta$, $\bar{\mu} = \mu/k_BT$, $\bar{E} = E/k_BT$, $\bar{\Omega}_* = \Omega_*/k_BT$, $\bar{G}_* = G_*/k_BT$, and $\bar{\Omega}_b = \Omega_b/k_BT$ leading to $\bar{\mathcal{V}} = \mathcal{V}\delta/D_o$, which defines the GB Péclet number. By integrating Eq. (5) once using the far-field boundary

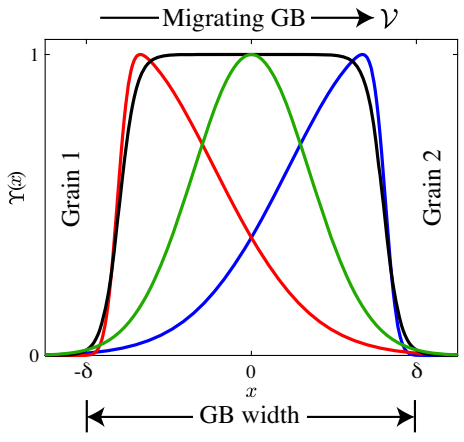

FIG. 1. The four Υ functions used to describe GB-solute interactions. The Gaussian (green), smoothed boxcar (black), left-(blue), and right-skewed (red) functions.

condition $c \to c_\infty$ as $x \to -\infty$, we obtain $\Upsilon c(1-c)\partial\bar{\mu}/\partial\bar{x} = -\bar{\mathcal{V}}(c-c_\infty)$, which, upon using Eq. (4), yields the following governing equation for the concentration field:

$$\frac{\partial c}{\partial \bar{x}} = \frac{g_1 c^3 + g_2 c^2 + g_3 c + \bar{\mathcal{V}} c_\infty}{g_4(c^2 - c) + g_5}, \tag{6}$$

where $g_1 = -2\bar{\Omega}_* \Upsilon\Upsilon'$, $g_2 = (2\bar{\Omega}_* - \bar{G}_*)\Upsilon\Upsilon'$, $g_3 = \bar{G}_* \Upsilon\Upsilon' - \bar{\mathcal{V}}$, $g_4 = 2\Upsilon(\bar{\Omega}_* \Upsilon + \bar{\Omega}_b)$, and $g_5 = \Upsilon$. Here, $(\cdots)' = d(\cdots)/d\bar{x}$. Next, the solute drag pressure P_d that the migrating GB experiences can be expressed in nondimensional form $\bar{P}_d$ as [13]

$$\bar{P}_d = \frac{P_d v_a}{k_B T} = -\int_{-\infty}^{\infty} (c - c_\infty) \frac{d\bar{E}}{d\bar{x}} d\bar{x}, \tag{7}$$

where v_a is the atomic volume. Equation (6) was solved numerically [34–36], where we simulated the concentration fields for all four Υ functions employed in this Letter and using a far-field bulk concentration $c_\infty = 0.05$, 0.1, and 0.2. Further, we used $\bar{\mathcal{V}} \in [0, 100]$, $\bar{\Omega}_{\mathrm{GB}} \in [-8.25, 0]$, and $\bar{\Omega}_b \in [0.75, 1.75]$ in steps of 0.1, 0.25, 0.25, respectively. Once the concentration fields were obtained, Eq. (7) was numerically integrated to obtain solute drag $\bar{P}_d$ as a function of $\bar{\mathcal{V}}$ and $\bar{\Omega}_*$.

Results.—The goal of this Letter is to explore GB segregation and solute drag in binary metallic alloys that are representative of experimentally observed ones, i.e., immiscible alloys with large solute concentration levels [17,18,24]. As a demonstration, we explore an alloy with $c_\infty = 0.1$, and we let $\bar{G}_* = -\bar{\Omega}_*$, indicating that the GB energy in pure A is comparable in magnitude to the one in pure B. Figure 2 shows a plot of concentration profiles for the four Υ functions used in this Letter for $\bar{\mathcal{V}} = 0$, 4, and 12 and using $(\bar{G}_*, \bar{\Omega}_*, \bar{\Omega}_b) = (5.75, -5.75, 0.75)$. For stationary GBs, our concentration profiles reproduce the exact solution to Eq. (5) with $\bar{\mathcal{V}} = 0$ [34]. It can be seen that the form of Υ influences both the concentration profile within the GB region and the depleted zone ahead of the migrating GB. It is also interesting to note that the functional form of Υ serves to break the symmetry in the concentration profiles. This can be seen in the cases with the left- and right-skewed Υ functions at $\bar{\mathcal{V}} = 0$, where the concentration is asymmetric across the GB. $\bar{\mathcal{V}}$ plays a similar role, in which increasing $\bar{\mathcal{V}}$ breaks the symmetry in concentration profiles as in the cases with the symmetric boxcar and Gaussian functions in Fig. 2. Further, while the left- and right-skewed Υ functions used in this Letter have the same structure except for a mirror reflection about $x = 0$, they exhibit drastically different concentration profiles across the migrating GB. For the case with the right-skewed function, solutes segregate to the trailing end of the migrating GB and, thus, a high level of solutes is maintained within the GB region. In contrast, the system with the left-skewed function shows that solutes segregate to the leading end of the migrating GB and, as a result, the GB experiences a large drop in solute concentration with increasing $\bar{\mathcal{V}}$. Next, we explore the resultant GB solute drag pressure, where Fig. 3(a) shows surface plots of solute drag

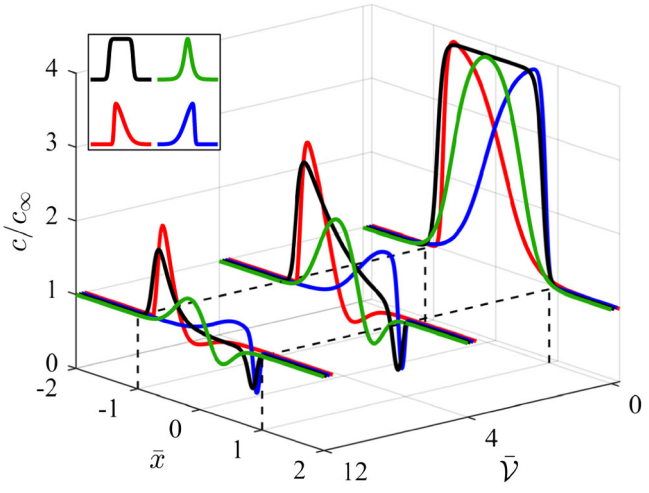

FIG. 2. Solute concentration profiles across the GB for $\bar{\mathcal{V}} = 0$, 4, and 12 for the four Υ functions used in this work. Here, we set $(c_\infty, \bar{\Omega}_b, \bar{\Omega}_*, \bar{G}_*) = (0.1, 0.75, -5.75, 5.75)$.

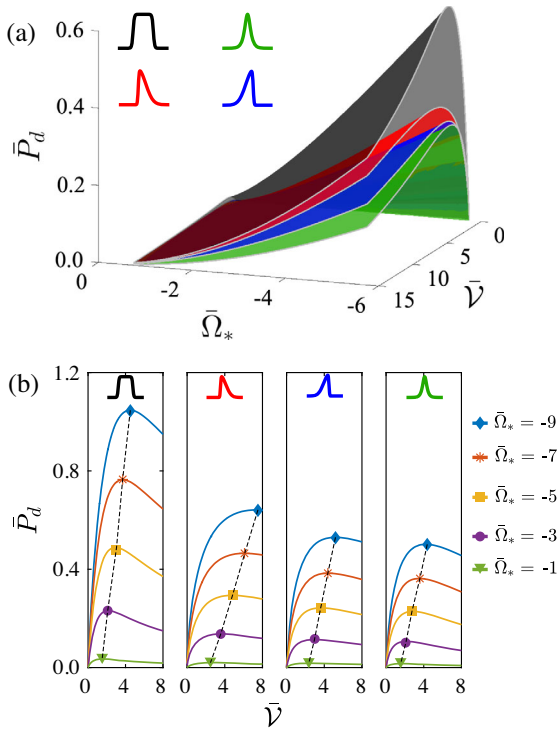

FIG. 3. For the four Υ functions used in this work: (a) A surface plot depicting solute drag $\bar{P}_d$ as a function of $\bar{\Omega}_*$ and $\bar{\mathcal{V}}$. (b) Slices of the $\bar{P}_d$ surface for various $\bar{\Omega}_*$ values depicting the shift in the maximum solute drag to larger $\bar{\mathcal{V}}$ with decreasing $\bar{\Omega}_*$. In both panels, $(c_\infty, \bar{\Omega}_b) = (0.1, 0.75)$.

$\bar{P}_d$ as a function of $\bar{\Omega}_*$ and $\bar{\mathcal{V}}$ using $(c_\infty, \bar{\Omega}_b, \bar{G}_*) = (0.1, 0.75, -\bar{\Omega}_*)$. It can be seen that solute drag increases rapidly with decreasing $\bar{\Omega}_*$. Again, $\bar{\Omega}_* < 0$ represents immiscible alloys and/or systems with GBs that favor *A*-*B* mixing. Indeed, the trends depicted in Fig. 3(a) are consistent with experimental observations, in which stagnant grain growth was observed in a wide range of immiscible alloys [17,18,24]. An interesting effect emerges in regular solution alloys, which deals with the location of the peak point in solute drag–velocity curves. Figure 3(b) shows slices of the $\bar{P}_d$ surface as a function of $\bar{\mathcal{V}}$ for various values of $\bar{\Omega}_*$, where it can be seen that decreasing $\bar{\Omega}_*$ shifts the peak point in solute drag to larger $\bar{\mathcal{V}}$ values, thus, extending the regime where solute drag is effective in mitigating GB migration. A closer examination of Fig. 3 suggests a self-similar behavior of solute drag, in which $\bar{P}_d$ can be cast in a functional form as

$$\frac{\bar{P}_d}{\bar{P}^*} = G_{\text{ref}}(\bar{\mathcal{V}}/\bar{\mathcal{V}}^*), \tag{8}$$

where $\bar{P}^* = \bar{P}^*(\bar{\Omega}_*)$ encompasses the role of bulk and GB heat of mixing in the maximum value of solute drag, and G_{ref} is a reference function of the rescaled $\bar{\mathcal{V}}/\bar{\mathcal{V}}^*$, describing the structure of the solute drag–velocity curve. $\bar{\mathcal{V}}^* = \bar{\mathcal{V}}^*(\bar{\Omega}_{\text{GB}}, \bar{\Omega}_b)$ is a characteristic velocity at the maximum drag pressure. For all simulated cases in this work, solute drag–velocity curves are rescaled by their respective $\bar{P}^*$ and $\bar{\mathcal{V}}^*$ values at the maximum point, and the results are shown in shaded gray lines in Fig. 4(a) for systems with $c_\infty = 0.05$, 0.1, and 0.2. The collapsed solute drag-velocity curves reveal a G_{ref} function that can be well fitted using

$$G_{\text{ref}} = \frac{1}{\left(\frac{\bar{\mathcal{V}}}{\bar{\mathcal{V}}^*}\right)} \exp\left[\frac{\lambda^2 - \left(\ln\left(\frac{\bar{\mathcal{V}}}{\bar{\mathcal{V}}^*}\right) - \lambda\right)^2}{2\lambda}\right], \qquad \frac{\bar{\mathcal{V}}}{\bar{\mathcal{V}}^*} > 0, \tag{9}$$

where $\lambda = 2.3 \pm 0.09$ is a fitting parameter. Figure 4(a) depicts a plot of G_{ref} [Eq. (9)] for the alloys with $c_\infty = 0.05$ (red circles), 0.1 (solid black line), and 0.2 (green triangles), demonstrating that Eq. (9) provides a robust fit to all solute drag profiles. Figures 4(b)–4(c) show, respectively, a plot of $\bar{P}^*$ and $\bar{\mathcal{V}}^*$ for the alloy with $c_\infty = 0.1$, where it can be seen that the maximum solute drag $\bar{P}^*$ scales with $\bar{\Omega}_*$ (i.e., $\bar{P}^* \propto \bar{\Omega}_*$) for all Υ functions explored in this Letter. This behavior can be understood by substituting the expression for $\bar{E}$ in Eq. (7) to yield [34]

$$\bar{P}_d = \bar{G}_* \int_{-\infty}^{\infty} (c - c_\infty)\Upsilon' d\bar{x} - \bar{\Omega}_* \int_{-\infty}^{\infty} (c^2)'\Upsilon d\bar{x}, \tag{10}$$

where it is evident that $\bar{P}_d$ scales with $\bar{\Omega}_*$ as in the case with $\bar{G}_* = -\bar{\Omega}_*$ depicted in Fig. 4(b). It is interesting to note that the first integral on the right-hand side of Eq. (10) corresponds to the solute drag predicted by Cahn [13] for ideal and dilute alloys. However, an additional contribution to solute drag, given by the second integral on the right-hand side of Eq. (10), emerges in regular solution alloys, which depends on the structure of the Υ function rather than its spatial gradient. This indicates that asymmetric Υ profiles introduce an additional component to solute drag that scales with $\bar{\Omega}_*$. This can be seen in Fig. 4(b), where solute drag in systems with the skewed Υ functions differs from the one with symmetric Gaussian Υ profile, and that this difference grows with decreasing $\bar{\Omega}_*$ values. Next, Fig. 4(c) shows a plot of $\bar{\mathcal{V}}^*$ as a function of the heat of mixing model parameters for the alloy with $c_\infty = 0.1$. An interesting effect can be seen in which the location of maximum solute drag shifts to larger velocities according to $\bar{\mathcal{V}}^* \propto (\bar{\Omega}_* + \bar{\Omega}_b) = \bar{\Omega}_{\text{GB}}$. This is an indication that negative GB heat of mixing $\bar{\Omega}_{\text{GB}}$ plays a stabilizing role in which decreasing $\bar{\Omega}_{\text{GB}}$ shifts the maximum solute drag to large velocities, thus, expanding the stability region (i.e., drag increases with GB velocity) due to solute drag. Finally, we compare our solute drag values with the intrinsic driving force for curvature-driven GB migration $\Delta P = \gamma_{\text{GB}}\mathcal{K}$ in some of the recently observed thermally stable nanocrystalline alloys. Using $\gamma_{\text{GB}} = 1$ J/m^2, operating temperature of $T = 800 - 1000$ K, atomic volume $v_a = 1.0$–3.0 Å^3, and assuming a grain size in the range

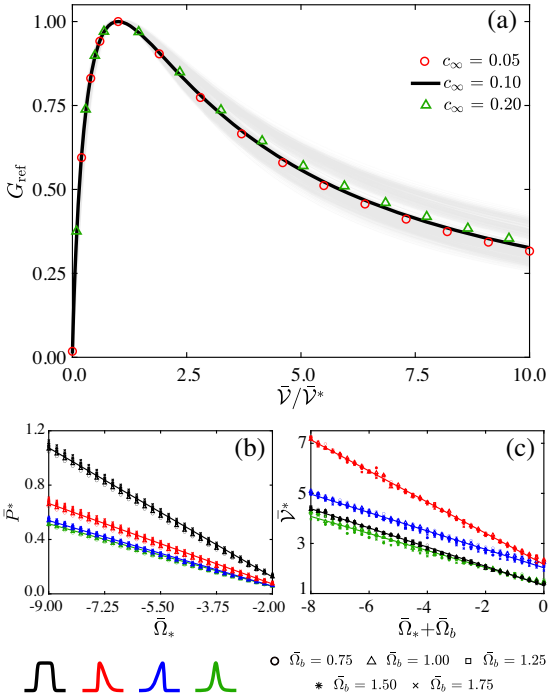

FIG. 4. (a) A plot of the proposed form for G_{ref} [Eq. (9)] along with the collapsed solute drag-velocity curves (gray lines) for alloys with $c_\infty = 0.05$, 0.1, and 0.2 and using the four Υ functions employed in this work. Using Eq. (8), a plot of (b) $\bar{P}^* = \bar{P}^*(\bar{\Omega}_*)$, and (c) $\bar{\mathcal{V}}^* = \bar{\mathcal{V}}^*(\bar{\Omega}_{\text{GB}}, \bar{\Omega}_b)$ for the alloy with $c_\infty = 0.1$ for various values of the bulk heat of mixing $\bar{\Omega}_b$.

of 50–100 nm resulting in mean curvatures $\mathcal{K} \approx 4\text{–}8 \times 10^7$ m^{-1}, the nondimensional driving force for GB migration is $\Delta\bar{P} = \Delta P v_a / k_B T \approx 0.003\text{–}0.02$, which falls well within the maximum solute drag values $\bar{P}^*$ shown in Fig. 4(b).

Conclusions.—In this Letter, we presented a solute drag model in regular solution alloys that accounts, at a mesoscopic scale, for monolayer, multilayer, and asymmetrical segregation. One conclusion from our Letter is that the spatial details of GB-solute interactions play a critical role in the magnitude of solute drag, with the case of multilayer segregation resulting in the largest solute drag. The maximum solute drag was found to scale with $\bar{\Omega}_*$, which describes the deviation in the GB heat of mixing from that of the bulk grains. It was also found that the peak points in solute drag-velocity curves shift to larger GB velocities with decreasing $\bar{\Omega}_*$, i.e., attractive (repulsive) solute-solute interactions within the GB (bulk). This Letter motivates further explorations of GB solute drag effects in engineering alloys.

F. A. and M. A. would like to acknowledge support from the U.S. Army Research Office through the Young Investigator Program (award No. W911NF-20-2-0122) and NSF DMR No. 2114832. F. A. acknowledges fruitful discussions with Dr. Murray Daw, Dr. Enrique Martinez, and Dr. Joshua Bostwick at Clemson University.

*fabdelj@clemson.edu

[1] A. P. Sutton and R. W. Balluffi, *Interfaces in Crystalline Materials* (Oxford University Press, New York, 1995), ISBN 978-0-19-850061-2.
[2] E. O. Hall, Proc. Phys. Soc. London Sect. B **64**, 747 (1951).
[3] N. J. Petch, J. Iron Steel Inst. **174**, 25 (1953).
[4] L. Lu, Y. Shen, X. Chen, L. Qian, and K. Lu, Science **304**, 422 (2004).
[5] O. S. Ivanova and F. P. Zamborini, J. Am. Chem. Soc. **132**, 70 (2010).
[6] T. Frolov, S. V. Divinski, M. Asta, and Y. Mishin, Phys. Rev. Lett. **110**, 255502 (2013).
[7] P. Lejček, M. Šob, and V. Paidar, Prog. Mater. Sci. **87**, 83 (2017).
[8] J. L. Johnson and R. M. German, Metall. Mater. Trans. A **27**, 441 (1996).
[9] N. Hwang, Y. Park, D.-Y. Kim, and D. Yoon, Scr. Mater. **42**, 421 (2000).
[10] J. Burke and D. Turnbull, Prog. Metal Phys. **3**, 220 (1952).
[11] R. Kirchheim, Acta Mater. **50**, 413 (2002).
[12] J. Weissmüller, Nanostruct. Mater. **3**, 261 (1993).
[13] J. W. Cahn, Acta Metall. **10**, 789 (1962).
[14] M. Hillert and B. Sundman, Acta Metall. **24**, 731 (1976).
[15] B. K. VanLeeuwen, K. A. Darling, C. C. Koch, R. O. Scattergood, and B. G. Butler, Acta Mater. **58**, 4292 (2010).
[16] K. Darling, L. Kecskes, M. Atwater, J. Semones, R. Scattergood, and C. Koch, J. Mater. Res. **28**, 1813 (2013).
[17] C. M. Barr, S. M. Foiles, M. Alkayyali, Y. Mahmood, P. M. Price, D. P. Adams, B. L. Boyce, F. Abdeljawad, and K. Hattar, Nanoscale **13**, 3552 (2021).
[18] T. Chookajorn and C. A. Schuh, Acta Mater. **73**, 128 (2014).
[19] T. Frolov, K. Darling, L. Kecskes, and Y. Mishin, Acta Mater. **60**, 2158 (2012).
[20] A. Devaraj, W. Wang, R. Vemuri, L. Kovarik, X. Jiang, M. Bowden, J. Trelewicz, S. Mathaudhu, and A. Rohatgi, Acta Mater. **165**, 698 (2019).
[21] M. Mendelev and D. Srolovitz, Acta Mater. **49**, 589 (2001).
[22] K. Lücke and G. Gottstein, Acta Metall. **29**, 779 (1981).
[23] A. J. Detor and C. A. Schuh, Acta Mater. **55**, 371 (2007).
[24] K. Darling, B. VanLeeuwen, C. Koch, and R. Scattergood, Mater. Sci. Eng. A **527**, 3572 (2010).
[25] A. K. Da Silva, D. Ponge, Z. Peng, G. Inden, Y. Lu, A. Breen, B. Gault, and D. Raabe, Nat. Commun. **9**, 1 (2018).
[26] T. Frolov and Y. Mishin, Phys. Rev. B **85**, 224107 (2012).
[27] Y. Mishin, Acta Mater. **179**, 383 (2019).
[28] V. K. Gupta, D.-H. Yoon, H. M. Meyer III, and J. Luo, Acta Mater. **55**, 3131 (2007).
[29] P. R. Cantwell, M. Tang, S. J. Dillon, J. Luo, G. S. Rohrer, and M. P. Harmer, Acta Mater. **62**, 1 (2014).
[30] H. Xie, Q. Huang, J. Bai, S. Li, Y. Liu, J. Feng, Y. Yang, H. Pan, H. Li, Y. Ren *et al.*, Nano Lett. **21**, 2870 (2021).
[31] A. Azzalini, *The Skew-Normal and Related Families* (Cambridge University Press, Cambridge, England, 2013), Vol. 3.
[32] D. A. Porter and K. E. Easterling, *Phase Transformations in Metals and Alloys* (CRC Press, Boca Raton, 2009).
[33] A. Van der Ven, H.-C. Yu, G. Ceder, and K. Thornton, Prog. Mater. Sci. **55**, 61 (2010).
[34] See Supplemental Material at http://link.aps.org/supplemental/10.1103/PhysRevLett.127.175503 for (i) details of the numerical algorithm used to solve the solute transport equation, (ii) derivation of the exact solute concentration profile for stationary GBs, (iii) a general form for the solute drag expression in regular solution alloys, and (iv) supplemental results for GB concentration profiles as a function of various bulk concentrations.
[35] T. Steihaug and A. Wolfbrandt, Math. Comput. **33**, 521 (1979).
[36] L. F. Shampine and M. W. Reichelt, SIAM J. Sci. Comput. **18**, 1 (1997).